

JGR Solid Earth

RESEARCH ARTICLE

10.1029/2019JB017298

Key Points:

- Coupled multiphase flow and geomechanics of CO₂ storage-enhanced oil recovery in a faulted oilfield is investigated
- Effect of well location and flow rate variability on geomechanical signatures of bypassed oil and fault stability is quantified
- Effect of multiphase geomechanics on stress transfer from reservoir into overburden and basement is explained

Supporting Information:

- Supporting Information S1

Correspondence to:

B. Jha,
bjha@usc.edu

Citation:

Zhao X., & Jha, B. (2019). Role of well operations and multiphase geomechanics in controlling fault stability during CO₂ storage and enhanced oil recovery. *Journal of Geophysical Research: Solid Earth*, 124. <https://doi.org/10.1029/2019JB017298>

Received 2 JAN 2019

Accepted 7 JUN 2019

Accepted article online 13 JUN 2019

Role of Well Operations and Multiphase Geomechanics in Controlling Fault Stability During CO₂ Storage and Enhanced Oil Recovery

Xiaoxi Zhao¹ and Birendra Jha¹ 

¹Department of Chemical Engineering and Materials Science, University of Southern California, Los Angeles, CA, USA

Abstract CO₂ injection in active oil fields is a technology proposed for industrializing carbon storage operations. However, monitoring CO₂ migration, oil recovery, and mechanical deformation within caprock and on faults is a challenging problem in large-scale storage-enhanced oil recovery operations due to intersecting faults, multiphase flow effects, and wells with complex production-injection schedule. We develop and demonstrate a methodology based on our coupled modeling framework to monitor the movement of CO₂, hydrocarbons and water, and the associated evolution in mechanical stability of faults during CO₂ storage-enhanced oil recovery in the Farnsworth Unit oil field in Texas, United States. The methodology honors geological, geophysical, and production-injection data acquired in the field over six decades. Differential depletion from hydraulically isolated fault compartments followed by water and CO₂ injection-induced overpressure causes volumetric contraction and expansion of the reservoir, and changes in the total and effective stresses in the overburden-reservoir-underburden complex. CO₂ migrates upward to accumulate near top of the geologic structure, and water migrates downward to pressurize the faults. Three-dimensional changes in the pressure and stress fields in the system lead to changes in the shear and effective normal tractions on three major faults compartmentalizing the field. Evolution in fault tractions is used to compute the evolution in the Coulomb failure function of the faults to quantify induced-slip tendency under production and injection. We explain the spatial heterogeneity and time variability of Coulomb failure function in terms of well location heterogeneity and well rate variability.

1. Introduction

It is known that production or injection of fluids in subsurface reservoirs can change stress inside and outside the reservoir. Such changes may perturb mechanical equilibrium and cause slip on the preexisting faults or trigger earthquakes (Albano et al., 2017; Evans et al., 2012; Segall, 1989; Segall & Fitzgerald, 1998; Segall & Lu, 2015; Won-Young, 2013; Won & Paul, 2016; Yerkes & Castle, 1976). Coupling between fluid flow and mechanical deformation in porous media has been used in recent studies for assessment of fault activation and induced seismicity (Fan et al., 2016; Jha & Juanes, 2014; Juanes et al., 2016; Panda et al., 2018). Various coupled multiphysics numerical simulation frameworks have been proposed for poroelastic media with mechanical discontinuities such as faults and fractures (Fan et al., 2016; Garipov et al., 2016; Mainguy & Longuemare, 2002; Minkoff et al., 2003). However, it still remains a challenge to apply such modeling and simulation frameworks to real fields with complex structural and stratigraphic features, for example, intersecting faults and layers, petrophysical heterogeneity, and time-dependent and spatially distributed production and injection. There is an urgent need to develop coupled modeling frameworks that can efficiently handle realistic geology, heterogeneous properties, and complex well schedules.

Injection and storage of CO₂ in depleted oil reservoirs is a technology that could reduce greenhouse gas emissions while enhancing the recovery of hydrocarbons (Franklin, 2009; Lackner, 2003; Szulczewski et al., 2012) from the oil field. However, injection-induced pressurization, simultaneous movement of CO₂ and hydrocarbon phases, and sudden changes in fluid compressibility due to CO₂ dissolution in oil (Ampomah et al., 2016) can lead to changes in the stress within and around the reservoir. This could potentially cause irreversible changes in the poromechanical properties of the rock, opening of fractures, or activation of critically stressed existing faults. Such changes may affect the oil recovery, create undesired pathway for CO₂ leakage, or induce seismic events (Bissell et al., 2011; Chiaramonte et al., 2008; Castelletto et al., 2013; Olden et al., 2012; Preisig & Prévost, 2011; Rutqvist et al., 2007, 2008; Streit & Hillis, 2004;

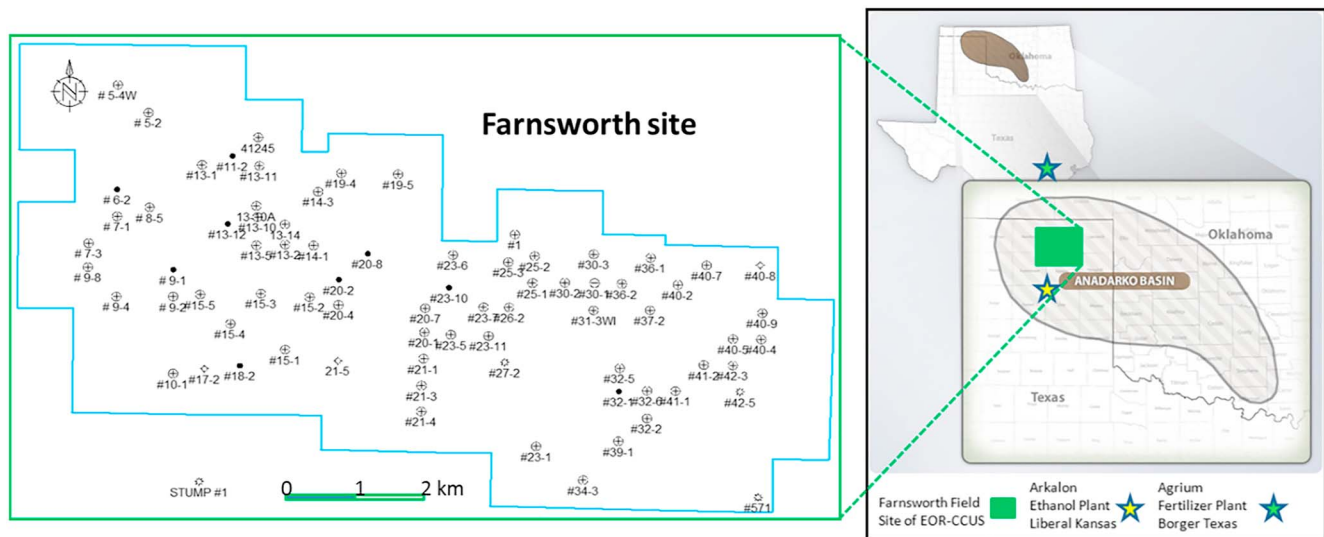


Figure 1. Map of the Farnsworth Unit (FWU) field. (Left) The border of FWU and some of the well locations are shown. (Right) FWU is located in the northern Texas within the Anadarko Basin (shaded region), and it is shown within a green square. The main source of anthropogenic CO₂ used during injection is highlighted by two star-shaped symbols: the northern star is the Arkalon Ethanol Plant in Liberal, Kansas, and the southern star is the Agrium Fertilizer Plant in Borger, Texas.

Teatini et al., 2014; Verdon et al., 2011; Vidal-Gilbert et al., 2009, 2010). Thus, it is important to monitor the flow and mechanical behavior of the overburden-reservoir-basement storage complex during CO₂ injection and oil production. Here, we report results from a coupled multiphase flow-geomechanical modeling and monitoring study of the Farnsworth Unit (FWU) oil field of Texas to understand the evolution of pressure, oil saturation, and stress in the storage complex and to monitor the mechanical stability of reservoir-intersecting faults.

2. FWU Geology

The FWU field is located in Ochiltree County, Texas, which is on the northeast shelf of the Anadarko Basin (Figure 1; El-kaseeh et al., 2017). The Upper Morrow Sandstone, which is the focus of this study, consists of 115- to 150-m-thick Morrow Shale and discontinuous coarse-grained Morrow-B Sandstone. The Morrow-B Sandstone layers with typical thicknesses between 6.7 and 15.2 m create the hydrocarbon-bearing reservoir. Conformably overlying the Upper Morrow is the Thirteen Finger Limestone and the lowest member of the Pennsylvanian Atoka Series. The base of Thirteen Finger Limestone consists of a thin coal bed overlain by fine crystalline dolomitic limestones and shales. Morrow Upper Shale and Thirteen Finger limestone serve as the caprock formations in FWU. Faulting in the FWU closely resembles the deformation in the nearby Wichita Megashift zone, which is a major sinistral strike-slip fault system in the foreland of the Amarillo-Wichita Mountain Front in the southern Anadarko Basin (Evans, 1979). The Wichita Megashift experienced vertical block movement followed by lateral strike-slip movement. The vertical fault movement is expressed as normal faults with a southward displacement (Ampomah et al., 2016). The left lateral strike-slip movement created anticline folding. A total of nine faults were interpreted from 3-D surface seismic data in FWU (Figure 2). Faults 1 through 5 are interpreted as part of a sinistral wrench fault system. Except fault 6, all faults intersect both Morrow-B Sandstone and Thirteen Finger Limestone.

The FWU was discovered in 1955 and unitized in 1963. Water injection-based secondary recovery commenced in 1964. Between 1955 and 2010, approximately 38 million stock tank barrels (MMstb, 1 stb = 0.159 m³) of oil and 28,000 standard cubic feet (Mscf, 1 scf = 0.0283 m³) of natural gas was produced from FWU. CO₂ injection started in December 2010 as part of tertiary recovery in the oil field, and it was implemented through five-spot well patterns. Since 2013, three to five new well patterns have been added each year for CO₂ storage-enhanced oil recovery (Figure 1 above and Figure S2 in the supporting information). Anthropogenic CO₂ is injected at a rate of about 518 tonnes/day or about 0.2 million metric tonnes/year. During October 2010 to July 2016, 13 injectors injected more than 0.8 million metric tonnes of CO₂, which helped to recover additional 1.5 million barrels (MMbbls) of oil from FWU.



Figure 2. Map view showing the faults within Farnsworth Unit (FWU) at the Morrow Sandstone depth level. The FWU boundary is shown with thick black lines. Township and range boundaries are shown in a light gray color. Nine faults are interpreted using FWU's 3-D seismic survey. Except fault 6, all other faults intersect both the Morrow-B Sandstone and Thirteen Finger Limestone.

3. Numerical Model

Using available seismic and well logging information in FWU, we create a 3-D geological model of reservoir-overburden-underburden system. In this study, we focus on the western part of FWU because CO₂ injection is confined to that region. Three major stratigraphic horizons are considered in the model: Morrow Shale Top, Morrow-B Sandstone Top, and Morrow-B Sandstone Base as shown in Figure 3. Morrow shale serves as the caprock while Morrow-B sandstone is the reservoir layer subjected to production and injection. The depth of each horizon is estimated by averaging the well marker depths from logs (see Figures S1 and S3; Ampomah et al., 2016; Balch et al., 2017). These depths are shown in Figure 3 along a cross-section A-A' defined in Figure 2. Three major faults compartmentalizing mechanical and hydraulic response of the oil field are included in the model.

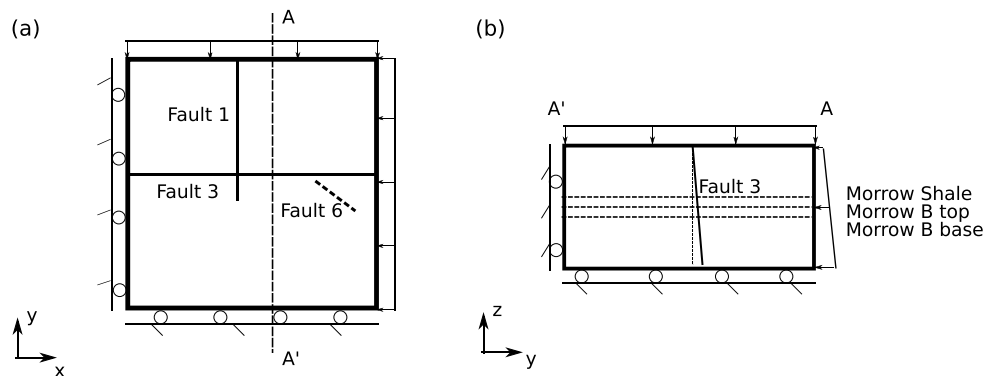


Figure 3. (a) Top view and (b) side view along cross-section AA' show the model geometry and the mechanical boundary conditions. Faults 1 and 3 are cutting through the model while fault 6 ends below the reservoir layer. Fault 3 is located near the center of the model and dips toward south with a 6° angle as shown in (b). Three major surfaces from the Morrow formation are highlighted in (b). (a) The minimum principal stress is applied on the y-positive surface. The maximum principal stress is applied on the x-positive surface. (b) A normal compression equal to the overburden is applied on the top boundary.

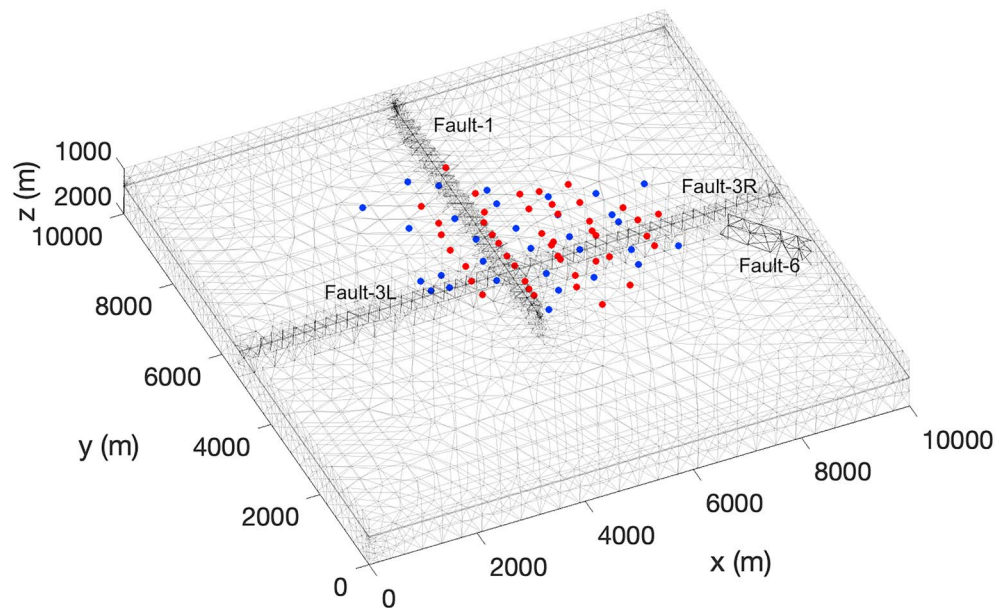


Figure 4. Computational domain mesh showing the locations of the fault surfaces and the wells. We use tetrahedral elements with smaller-sized elements within the reservoir layers and next to the fault surfaces and larger-sized elements near the domain boundaries. Fault 3 is broken into fault 3L (western part) and fault 3R (eastern part). Injectors are shown with blue dots, and producers are shown with red dots.

3.1. Mesh

The model dimensions are $10 \text{ km} \times 10 \text{ km} \times 1 \text{ km}$ in x , y , and z directions. The depth interval of the model is from $z = 1 \text{ km}$ to $z = 2 \text{ km}$ below the ground surface. Three major faults are considered: faults 1, 3, and 6. According to White et al. (2017), fault 3 is almost vertical with a small dip to the south. We assume the dip angle to be 6° as shown in Figure 3. Similarly, fault 1 is bending to west with an angle of 6° . Both faults 1 and 3 cross through the three horizons. However, fault 6 is younger, that is, more recent than Morrow-B Sandstone, and terminates just below the reservoir. We assume fault 6 to be vertical based on regional geology. Since faults 1 and 3 are intersecting with each other, they will share the same grid elements around the intersection region. Thus, for these elements, it is difficult to determine which fault movement to follow during simulations of fault slip. We address this situation by splitting fault 3 into two smaller faults, faults 3L and 3R, in the model. The resulting gap between faults 3L and 1 and between faults 3R and 1 is approximately 350 m long (it is smaller in the refined mesh described in the supporting information). Fluids can move through the gap to establish partial hydraulic communication across the faults, which is also supported by a previous flow simulation study in FWU (Ampomah, Balch, Cather, Rose-Coss, & Gragg, 2017).

Conformal 3-D meshing of a domain containing multiple arbitrarily-shaped and intersecting surfaces is a computational challenge and an open research problem. According to one estimate (SpaceClaim, 2018), analysts can spend more than 75% of their time trying to simplify and work with complex geometric objects prior to meshing. The fault meshing challenge has led to exclusion of many (Juanes et al., 2016) or all (Hornbach et al., 2015; Lei et al., 2013) intermediate-scale faults, which are potential sources of induced seismicity, from prior modeling studies. We developed a generalized meshing workflow that can honor intersections of multiple curved faults and layers in 3-D. Our workflow, which is implemented in Trellis (Trellis, 2017), has the following steps. First, we create nonuniform rational B-spline representation of fault surfaces and stratigraphic horizons. Then we build a 3-D solid geometry of faults/horizons using defeaturing and topological operations of webcut, chop, trim, merge, and imprint to create hanging and footwall fault blocks and layers in the reservoir, overburden, and underburden. We remove small-scale features that cause failure of the meshing algorithm. We use a bottom-up meshing approach in which 1-D curve objects of a horizon or a fault surface are meshed first followed by meshing of the parent 2-D object. Meshing of a selected number of 2-D surfaces in a 3-D fault block guides the meshing of the 3-D block itself, which is followed by meshing of the entire 3-D solid volume. We use tetrahedral elements to honor arbitrary 3-D geometry of faults and achieve conformance between the mesh and the geologic structure of the region. This increases the accuracy

of fault stresses predicted to result from CO₂ injection and hydrocarbon production. We use adaptive meshing to generate coarser mesh near the domain boundaries and in hydraulically inactive regions, and finer mesh within active flow regions, for example, within thin reservoir layers, and around wells and faults. This reduces the total number of mesh elements and enables faster simulations. This model has a total of 33,760 tetrahedral elements as shown in Figure 4. The average element volume is approximately $1.8 \times 10^5 \text{ m}^3$ in the reservoir and $3.6 \times 10^6 \text{ m}^3$ outside of the reservoir. To analyze the mesh sensitivity of the results and conclusions, we created a finer mesh of the domain with 261,207 elements that is described in the supporting information. Consistent finite element and finite volume mesh files are created from both meshes to provide input to the coupled simulator.

3.2. Fault Model

There are two stages in fault modeling: mesh representation and dynamic failure of faults. The finite element mesh is processed to introduce zero thickness interface elements and cohesive nodes on each fault surface (Aagaard et al., 2013). This allows representing the fault as a surface of displacement discontinuity embedded in the continuum and calculation of the fault slip and traction vector components in the three directions—lateral along strike, along dip, and outward normal (Jha & Juanes, 2014).

We solve the nonlinear contact problem subject to the Mohr-Coulomb frictional failure condition at the fault cohesive nodes to model fault slip (Aagaard et al., 2013; Jha & Juanes, 2014). In this study, the FWU faults do not fail, which agrees with observations in the field. Our focus is on quantifying the likelihood of failure or the change in mechanical stability induced by production and injection. The likelihood of fault failure is assessed by evaluating the change in Coulomb failure function, ΔCFF , which is a function of the changes in pressure and stress around the fault (Jha & Juanes, 2014; Reasenbergs & Simpson, 1992):

$$\begin{aligned} \Delta\text{CFF} &= \text{CFF}(t) - \text{CFF}(0) = (|\tau| + \mu_f \sigma'_n)_t - (|\tau| + \mu_f \sigma'_n)_0 \\ &= \left[\left(\sqrt{\tau_{\text{lat}}^2 + \tau_{\text{dip}}^2} \right)_t - \left(\sqrt{\tau_{\text{lat}}^2 + \tau_{\text{dip}}^2} \right)_0 \right] + \mu_f [(\sigma'_n)_t - (\sigma'_n)_0] \\ &= \Delta|\tau| + \mu_f \Delta\sigma'_n = \Delta|\tau| + \mu_f (\Delta\sigma_n + b\Delta p_f). \end{aligned} \quad (1)$$

Above, $\Delta|\tau|$ is the magnitude of change in the shear traction vector, μ_f is the fault friction coefficient, $\Delta\sigma'_n = \Delta\sigma_n + b\Delta p_f$ is the change in effective normal traction, $\Delta\sigma_n$ is the change in total normal traction, and Δp_f is the change in fault pressure. Here, we consider tension to be positive and compression to be negative, so a positive ΔCFF indicates a destabilizing effect on the fault. We consider all shear to be destabilizing and use the magnitude of shear traction in ΔCFF calculation.

Use of interface elements to represent a fault allows us to reproduce the pressure jump across the fault, which is observed in the field as a difference in the flow rate and pressure in wells located across the faults that compartmentalize the reservoir. Because of the pressure discontinuity, fault stability can be assessed by evaluating the Coulomb failure criterion on both the hanging wall and the footwall sides of the fault separately. Since the failure criterion is met first with the larger of the two pressures, we define the fault pressure p_f to be the larger of the two pressures as proposed recently (Jha & Juanes, 2014; Jagalur-Mohan et al., 2018; Yang & Juanes, 2018).

The value of the Biot coefficient b can be high in fault zones. If b is assumed to represent an unconsolidated fault zone undergoing rupture, or if a conservative estimate of the induced event trigger time is desired, then b can take values near its upper limit, that is, $b = 1$ (Segall & Fitzgerald, 1998). We assume a uniform static friction coefficient value of $\mu_f = 0.6$ on all the faults. The friction coefficient value does not affect the results of this study because the faults do not slip, and we focus on the relative change in values of the state variables.

3.3. Petrophysical Properties

The model is populated with poromechanical properties obtained using two representative well logging data sets (see Figure S3 for one of the two data sets). Different reservoir properties are assigned along and across the layers to model anisotropic response. The average bulk density is $\rho_b = 2,480 \text{ kg/m}^3$, the average sonic compressional velocity is $V_p = 3,600 \text{ m/s}$, and the average sonic shear velocity is $V_s = 1,920 \text{ m/s}$. Dynamic values of the bulk modulus and Young's modulus can be calculated as follows:

$$K = \rho_b \left(V_p^2 - \frac{4}{3} V_s^2 \right), \quad E = \frac{\rho_b V_s^2 (3V_p^2 - 4V_s^2)}{V_p^2 - V_s^2}. \quad (2)$$

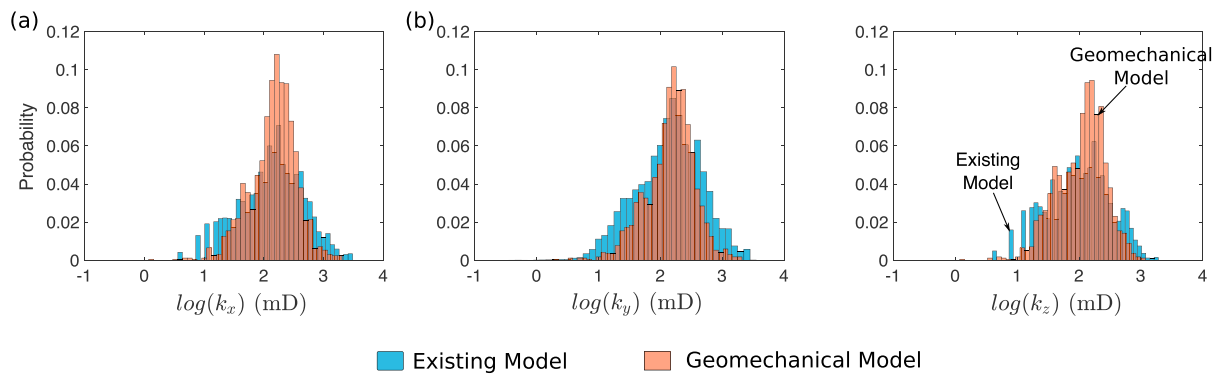


Figure 5. 3-D mapping of rock properties from an existing flow-only uncoupled model into the geomechanical model. Histograms of log-normalized permeability in (a) x direction, (b) y direction, and (c) z direction from the uncoupled Eclipse model (blue color) and the coupled geomechanical model (orange color).

The values are $K = 19.95$ GPa and $E = 23.79$ GPa. The Biot coefficient is assumed to be $b = 0.6$, which is representative of consolidated clastic formations in FWU.

Reservoir permeability values are obtained by mapping the permeability field of an older simulation model (Ampomah, Balch, Cather, Rose-Coss, Will, et al., 2017) on to the coupled geomechanical model. The older model is constructed in Eclipse (Schlumberger, 2017), is uncoupled to mechanics, and has been used to track CO_2 migration and oil recovery in FWU. Also, the uncoupled Eclipse model covers a smaller area and has smaller mesh elements compared to the coupled geomechanical model. As a result, the coupled model overlaps only partially with the uncoupled model. We average the property value of all the elements of the uncoupled model that are intersected by a coupled model element to obtain the property value of the coupled element. In the nonoverlapping region, the geomechanical elements are assigned the field-averaged value of the respective property.

Quality of the property mapping algorithm is evaluated by comparing the property histograms of the two models (Figure 5). We observe that the two histograms have similar values for the average permeability and the permeability variance. During model calibration, also known as history matching, we increased the permeability values by a factor of 3 to honor the historical production and injection rates and pressures. The average permeability in the x and y directions is approximately 189 mD ($1 \text{ mD} = 9.87 \times 10^{-16} \text{ m}^2$), and the average permeability in the z direction is approximately 144 mD. The permeability field is assumed to be constant in time. This is a reasonable assumption in Farnsworth because of the consolidated lithology of the formations and a relatively small change in the average reservoir pressure, which is actively maintained through waterflooding and CO_2 injection.

Pore volume is one of the key properties of any reservoir simulation model because it is related to the original hydrocarbon volume, ultimate recovery from primary depletion, and the rate of change in pore pressure due to production/injection. The pore volume is a product of porosity and the bulk volume of the reservoir. We assume a uniform initial porosity of 0.3 in the flow model. This honors the historical production

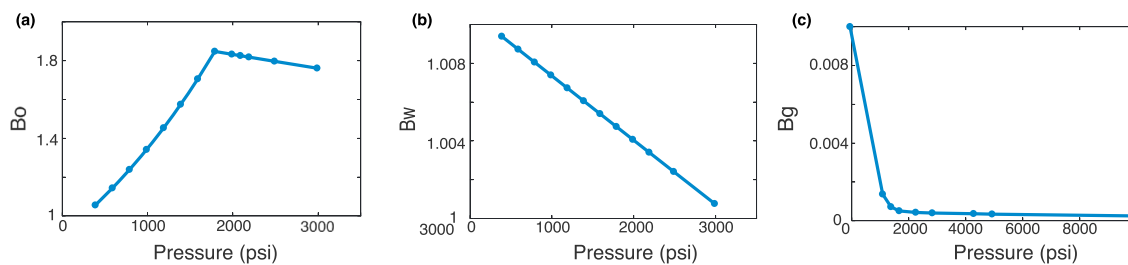


Figure 6. Formation volume factors for (a) oil, (b) water, and (c) gas phases. The bubble point pressure of oil is approximately 1,900 psi ($1 \text{ psi} = 6,894.76 \text{ Pa}$) below which dissolved gas is released from the oil phase. We assume a constant water compressibility, which corresponds to a constant dB_w/dp . We use CO_2 properties for the gas phase instead of the reservoir gas properties. This allows us to honor the CO_2 injection and transport behavior in the field more accurately.

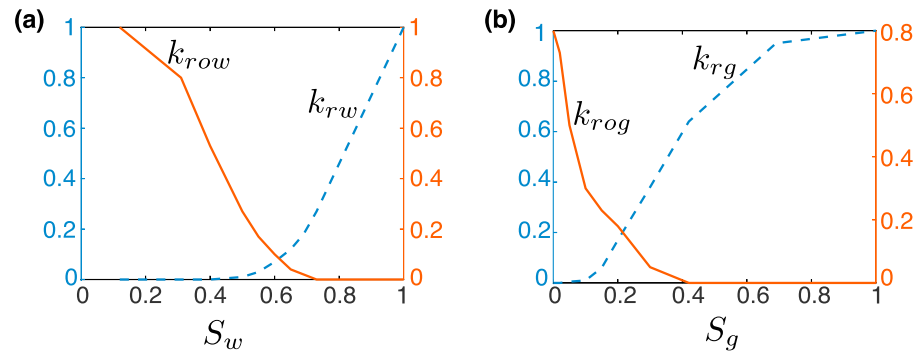


Figure 7. The three-phase (oil, water, and gas) relative permeability model in our simulation is based on two two-phase relative permeabilities. (a) Relative permeability of water k_{rw} (dash) and relative permeability of oil in presence of water k_{rown} (solid) as functions of the water saturation S_w . (b) Relative permeability of gas k_{rg} (dash) and relative permeability of oil in presence of gas k_{rong} (solid) as functions of the free gas phase saturation S_g . The relative permeability of oil k_{ro} is calculated dynamically during the simulation as a function of k_{rown} , k_{rong} , and the saturations.

and injection volumes and avoids complexity due to heterogeneity in the porosity field. The reservoir bulk volume is determined by the mesh structure.

We use a three phase-three component Black-Oil model (Aziz & Settari, 1979) to represent the multiphase flow system during flow simulation. The Black-Oil flow model must be initialized with phase-dependent fluid properties: compressibility, viscosity, and the dissolved phase volume fraction as functions of the fluid phase pressure. We provide these properties for oil, water, and gas phases that are representative of FWU fluids at reservoir conditions. The Formation Volume Factors of the fluid phases, which determine their compressibilities (Aziz & Settari, 1979), are plotted in Figure 6. The multiphase flow model is defined with saturation-dependent relative permeability tables for oil, water, and gas phases (Figure 7). The relative permeability curves for water (k_{rw}), for oil in presence of water (k_{rown}), for oil in presence of gas, (k_{rong}), and for gas (k_{rg}) are based on lab measurements and calibration of the Eclipse flow model to measured production volumes in the field. We use the segregation model to calculate the three-phase oil relative permeability (k_{ro}) as a function of k_{rown} , k_{rong} , and saturations of water and gas phases.

Transmissibilities of the three faults in the three directions (lateral shear, dip shear, and normal directions) are set to zero. Partial hydraulic communication across the faults exists through the gap between the faults as mentioned in the Mesh section above. This honors the fault gouge calculations (Hutton, 2015) and pressure observations in the field. Compared to the scenario with conductive faults, zero-transmissibility faults cause the reservoir pressure changes resulting from fluid injection and production to be larger. This induces larger changes in the fault stresses, which allows us to simulate a mechanically conservative scenario in the field with regard to the maximum allowable CO_2 injection pressure and storage capacity.

3.4. Initial and Boundary Conditions

The flow-geomechanical model is initialized under mechanical and hydrostatic equilibrium with normal faulting stress regime imposed via appropriate tectonic stresses at the boundaries. Following Ampomah et al. (2016), we set the initial oil saturation to 0.69 and the initial water saturation to 0.31 for the whole model. Based on Figure 7, the water phase is immobile at this saturation. The initial pressure follows the hydrostatic pressure gradient as expected based on initialization of the flow model (see Figure S4). The initial stress field is set to honor the oblique strike-slip normal faulting stress regime of fault 3, which strikes east-west. The minimum horizontal principal stress is assumed to be 0.9 times the maximum horizontal principal stress, which we assume to be equal to the vertical stress. The minimum stress is applied on the northern boundary (y -positive surface), and the maximum principal stress is applied on the eastern boundary (x -positive surface). The vertical stress is assumed to be lithostatic: $\sigma_v = -g \int \rho_b(z) dz$ (compression negative), where g is the value of gravitational acceleration. A normal compression equal to the overburden weight is applied on the top boundary at $z = 1$ km (Figure 3).

3.5. Production and Injection History

The coupled fluid flow and geomechanical simulation spans approximately 60 years of production and injection from January 1956 to July 2016. There are 76 wells in the field: 45 producers and 31 injectors (Figure 4).

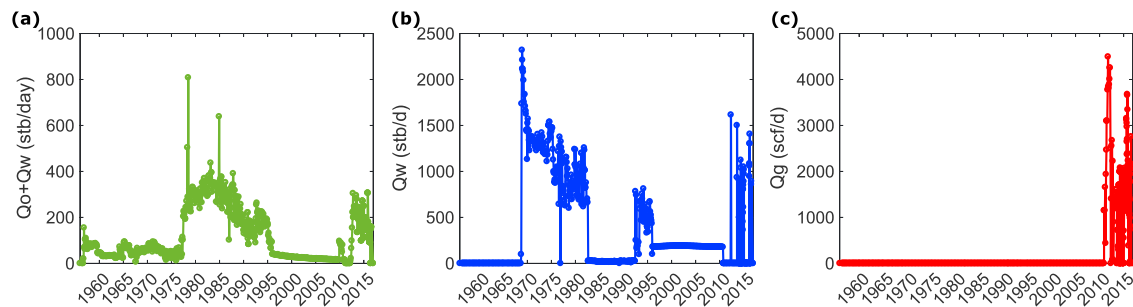


Figure 8. Typical production and injection rate profiles of Farnsworth Unit wells. (a) The liquid production rate ($Q_o + Q_w$, oil + water) of a producer, (b) the water injection rate Q_w of a water injector, and (c) the gas injection rate Q_g of a gas injector. Production starts at the beginning of the simulation. Water injection starts in year 1995. Gas injection starts in year 2010. Note the variability and discontinuity in the rate profiles, which will be related to fault stability patterns in the analysis below.

Production and injection profiles of typical production and injection wells are plotted in Figure 8. Cumulative liquid (oil and water) production at the end of the simulation is approximately 60 MMstb (million stock tank barrel). Water injection starts in year 1967, and the cumulative injection volume is approximately 70 MMstb. Gas injection starts in 2010, and the cumulative gas injection volume is approximately 30 MMscf (million standard cubic feet). Since the objective of this study is to identify the fault stability mechanisms arising out of the coupling between multiphase flow, geomechanics and well operation, we do not focus on matching these numbers on cumulative production and injection volumes exactly in our simulation.

4. Numerical Simulation

Production and injection history is used to drive the coupled simulation model through six decades of FWU development using our in-house simulator, Pylith-GPRS. The simulator has been described in detail (Jha & Juanes, 2014) and applied to a real oil field (Juanes et al., 2016), a gas field (Jha et al., 2015), an aquifer (Panda et al., 2018), and synthetic CO_2 sequestration cases (Castineira et al., 2015; Jagalur-Mohan et al., 2018). Here, we briefly reiterate the salient features of the simulator. The simulator solves the coupled system of nonlinear partial differential equations that model the physics of quasi-static mechanical equilibrium of the porous skeleton and conservation of mass for each fluid component (oil, water, and gas). This is a fully nonlinear, two-way coupled, multiphase geomechanics formulation (Coussy, 2004; Jha & Juanes, 2014). Fluid flow affects mechanical equilibrium through pressure-induced changes in the effective stress and fluid density-induced changes in the gravitational body force. Mechanical deformation affects fluid flow through the rate of volumetric stress, which changes the pore volume. We use an unconditionally stable scheme, the fixed stress scheme (Castelletto et al., 2015; Jha & Juanes, 2014; Kim et al., 2011), that solves the coupled system of discretized equations sequentially and iteratively till convergence at each time step. A flowchart summarizing the interaction among the models is provided in Figure 9.

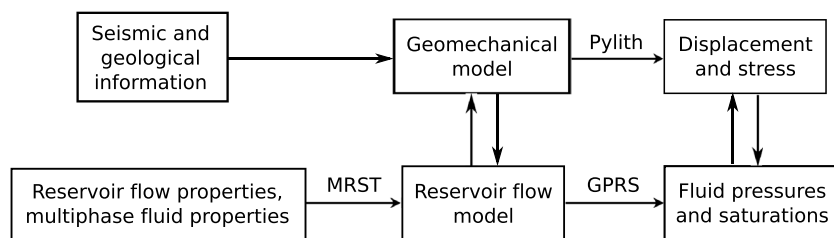


Figure 9. Flow chart showing the workflow and connections between different modules. Available seismic and geological information are used to construct a geomechanical model and populate it with poromechanical properties. Reservoir flow properties (porosity and permeability) and fluid properties (fluid density, viscosity, and compressibility) are obtained from an older uncoupled model and transferred to the geomechanical model using the Matlab Reservoir Simulation Toolbox (MRST; Lie, 2016). The flow-geomechanical simulator, PyLith-GPRS, outputs 3-D fields of the effective stress tensor, the displacement vector, fluid phase pressures, and saturations.

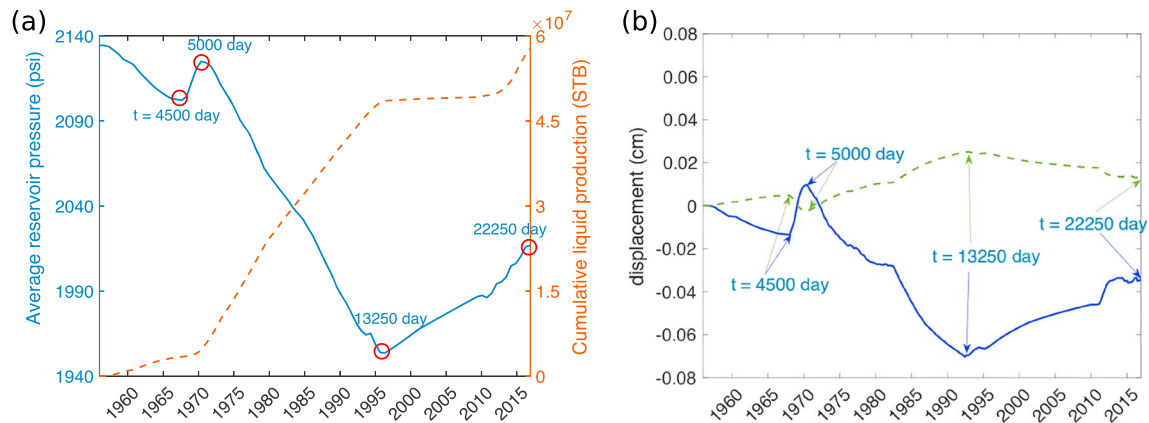


Figure 10. (a) Time evolution of the average reservoir pressure (psi) due to production, injection, and flow-induced stresses. The maximum pressure drop is approximately 200 psi. Cumulative liquid production is shown by the red dot curve. (b) Time evolution of the vertical displacement at two selected points on Morrow-B Top (blue line) and Morrow-B Base (green dash line). Vertical displacement on the two surfaces have opposite signs because of their opposite motion in response to volumetric contraction/expansion of the reservoir with pressure decrease/increase. Displacement at the reservoir bottom has smaller magnitude due to the zero displacement boundary condition at the bottom boundary of the model.

5. Results

5.1. Field Results

Evolution of the average pressure in the reservoir is plotted in Figure 10a. The average pressure remains almost constant in overburden and basement because they are hydraulically isolated from the reservoir. Small changes in overburden and basement pressures do occur due to undrained deformation caused by changes in the total stress due to bulk volume changes in the reservoir. The reservoir pressure decreases at the beginning of the simulation due to production. Around year 1966, injection begins, which leads to a temporary increase in the pressure. Since the total production flow rate is higher than the total injection flow rate, the reservoir pressure decreases thereafter. During 1995–2010, the production rate is curtailed for most of the producers while water injection continues at relatively high rates causing the average pressure to increase. CO₂ injection in year 2013 causes an increase in both production and pressure. The maximum pressure drop in the reservoir during the entire simulation is approximately 200 psi (1 psi = 6,894.76 Pa). We select four representative time steps—day 4,500 (year 1969), day 5,000 (year 1970), day 13,250 (year 1996), and day 22,250 (year 2016)—to further investigate the result.

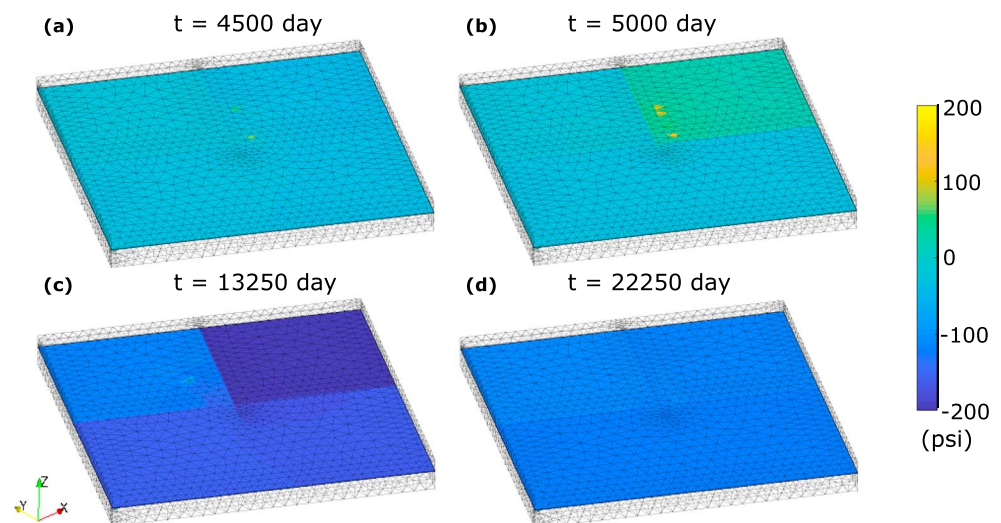


Figure 11. Changes in the reservoir pressure compared to the initial pressure at the four selected time steps: a, b, c, and d. Pressure decreases in regions with net production and increases in regions with net injection. The maximum pressure drop is 200 psi approximately and occurs around $t = 13,250$ day. The final pressure drop at $t = 22,250$ day is 150 psi approximately.

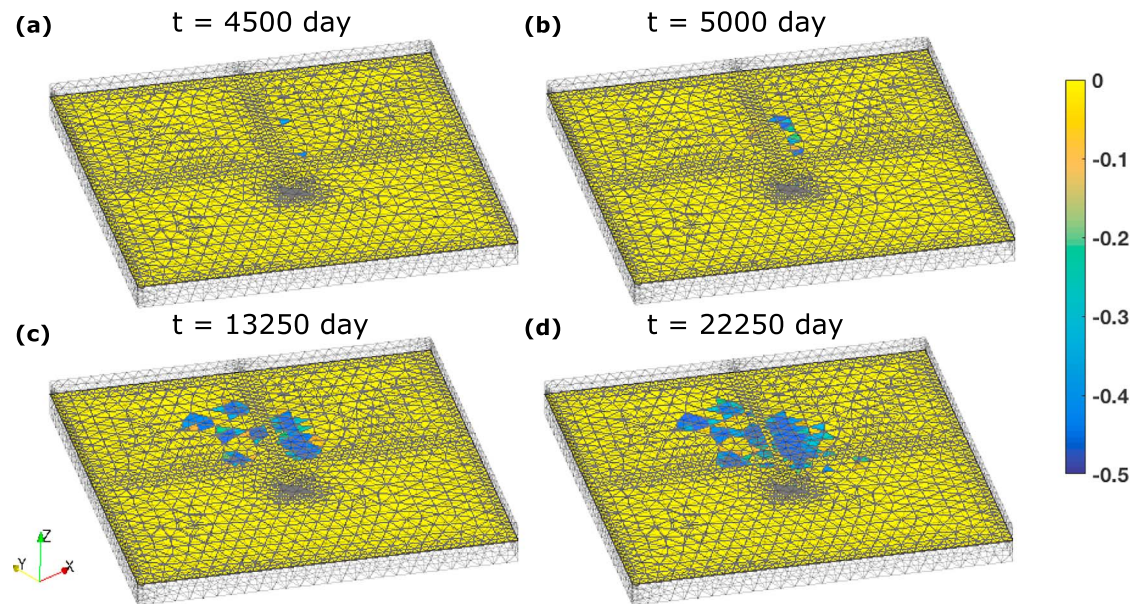


Figure 12. Changes in the oil saturation with respect to the initial oil saturation at the four selected time steps: a, b, c, and d. The oil saturation decreases around both producers and injectors, as expected. The maximum change in the saturation is approximately 0.5. The oil saturation remains almost unchanged in regions far from the wells, which suggests the presence of bypassed oil.

We show the evolution of vertical displacement at the reservoir boundaries in Figure 10b. The top boundary of the reservoir, Morrow-B Top, experiences downward and upward movements, that is, negative and positive vertical displacement, due to decreasing and increasing reservoir pressure, respectively. Morrow-B Base experiences movements in the opposite direction for the same pressure changes. The displacement magnitude is smaller at Morrow-B Base because of the zero displacement boundary condition at the bottom boundary of the model.

We plot 3-D fields of changes in the pressure and oil saturation for the reservoir region, that is, within the depth interval of 1,380–1,410 m (Figures 11 and 12). At $t = 0$ day, the changes in pressure and oil saturation with respect to their initial values are zero. For $0 < t < 4,500$ day, production leads to a drop in pressure

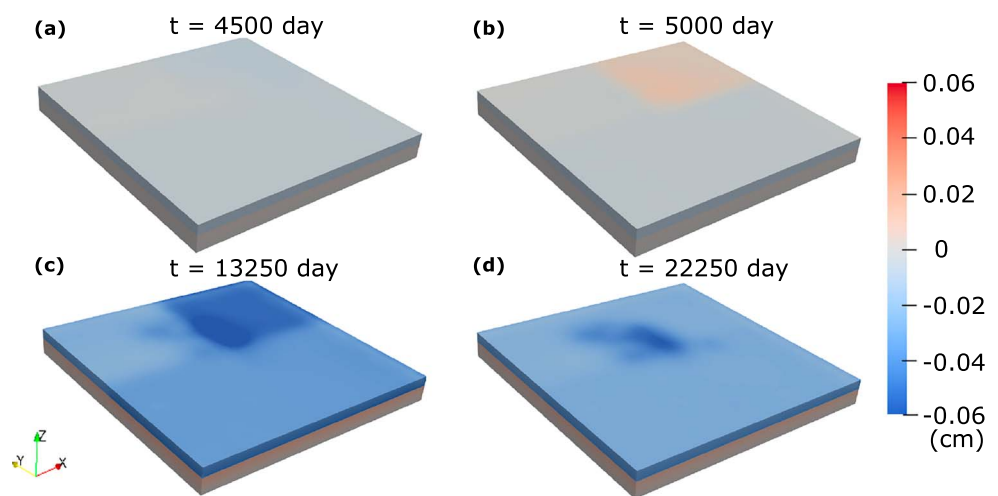


Figure 13. Vertical displacement field (centimeters) at the four selected time steps: a, b, c, and d. Pressure drop in the reservoir leads to negative (blue color) vertical displacement above the reservoir while pressure increase in the reservoir leads to positive (red color) vertical displacement above the reservoir. Below the reservoir, the vertical displacement shows opposite behavior as it experiences uplift during reservoir contraction and downward push during reservoir expansion. The asymmetry in the mechanical boundary conditions between the top (fixed traction) and bottom (fixed displacement) boundaries of the model affects the magnitude of vertical displacement.

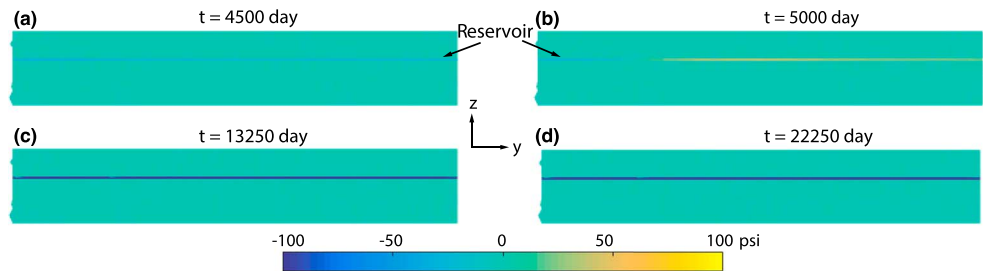


Figure 14. Change in the fault pressure (psi) along fault 1 at the four selected time steps: a, b, c, and d. A trend similar to that of Figure 11 can be observed. The fault pressure in the reservoir depth interval (appearing as a horizontal stripe) declines at early times due to production from both fault blocks. Later, it increases due to injection and then decreases again toward the end of the simulation due to net production.

within the reservoir. Small amount of injection happens in the northeast part of FWU causing an increase in pressure and a decrease in the oil saturation around those injection wells. At $t = 5,000$ day, the increase in pressure and the decrease in oil saturation in the northeast part are larger while the pressure continues to decrease in other parts of the reservoir. At $t = 13,250$ day, a pressure drop of 200 psi can be observed in the northeast part, while it is approximately 100–150 psi in the remainder of the reservoir. As more wells are brought on-line, the oil saturation continues to drop around those wells. At the end of the simulation, $t = 22,250$ day, the average pressure drop in the reservoir is approximately uniform at 150 psi, and the average drop in the oil saturation around the active wells is 0.5 approximately.

We want to identify the geomechanical signatures of reservoir compartmentalization and bypassed oil reserves due to the presence of faults, suboptimal well configurations, and processes such as high-permeability channeling and gravity segregation of CO_2 (Lake et al., 2015). We plot 3-D fields of the vertical displacement for the whole model over a depth interval of 1,000–2,000 m at the selected time steps (Figure 13). At $t = 0$ day, the model is at mechanical equilibrium, and all displacements are zero. Due to production-induced pressure depletion, the vertical displacement becomes negative (cause for subsidence)

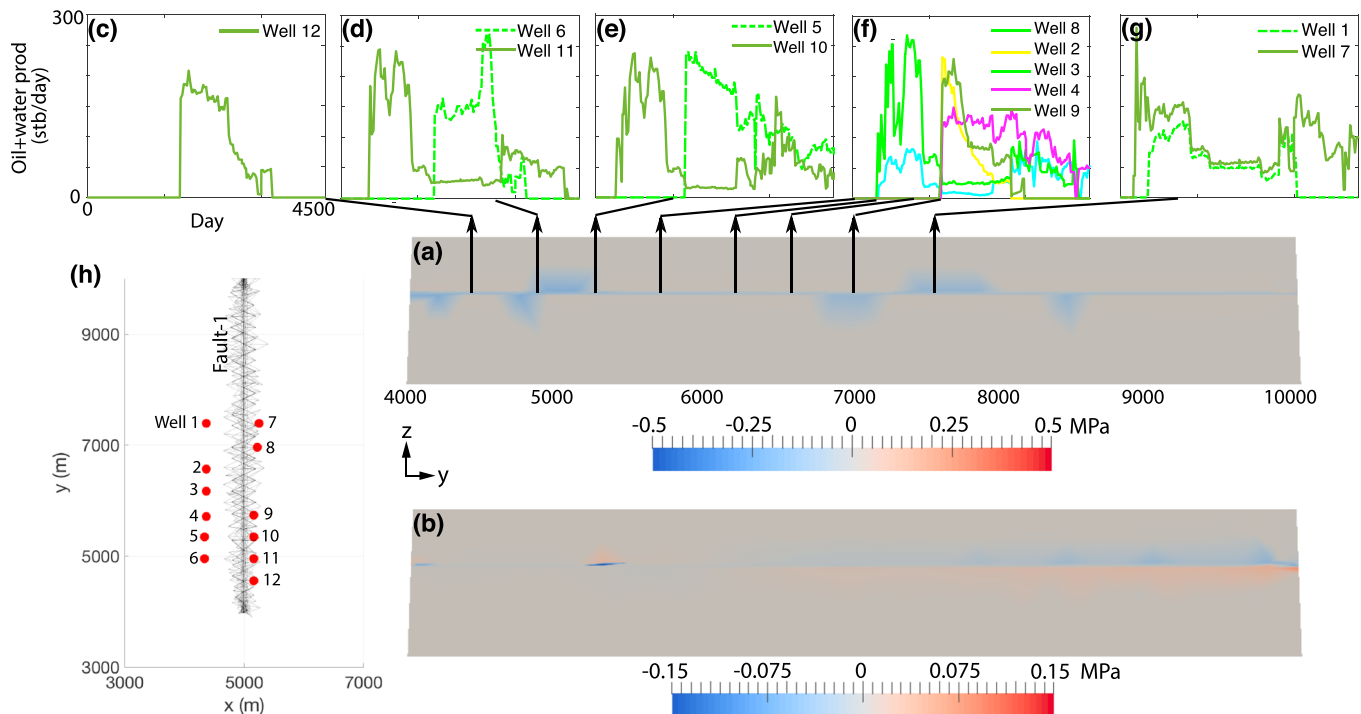


Figure 15. Effect of spatial distribution and temporal evolution of production on fault stability. Changes in (a) the effective normal traction and (b) the updip shear traction on fault 1 at $t = 4,500$ day with respect to the initial traction values. Liquid production profiles of active producers near fault 1 are shown in (c) through (g). Surface locations of the wells with respect to the fault are shown in (h).

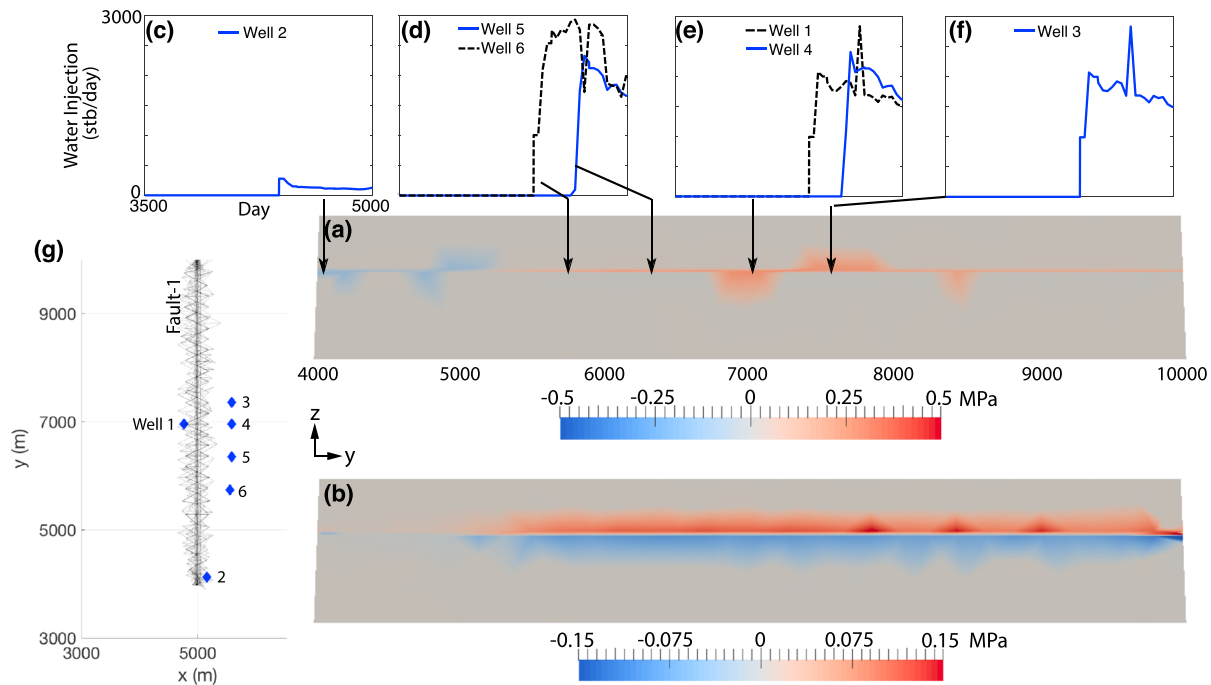


Figure 16. Effect of spatial distribution and temporal evolution of injection on fault stability. Changes in (a) the effective normal traction (megapascal) and (b) the updip shear traction (megapascal) on fault 1 at $t = 5,000$ day. Water injection in six wells, shown in (c) through (f) along the fault strike, causes updip shear above the reservoir (red color in b) and downdip shear below the reservoir (blue color in b). Tensile stresses are induced in the overburden and basement, which cause tensile changes in the effective normal traction (red color in a). Production dominates injection in the south, which causes compressive changes in the effective normal traction (blue color in a) near well 2. Surface locations of the wells with respect to the fault are shown in (g).

near the top of the model around 4,500 day. At 5,000 day, due to injection-induced pressure increase, the vertical displacement becomes positive (cause for uplift) in the northeastern part of the model where the injectors are located. At $t = 13,250$ day, negative vertical displacements can be seen above the reservoir while positive vertical displacements are seen below the reservoir. This is consistent with a volumetric contraction of the reservoir layers (Segall & Fitzgerald, 1998). At the end, the model shows a maximum subsidence of approximately -0.05 cm at the top boundary. The nontrivial shape of the displacement contours reflects the time-dependent and spatially variable flow rates of the FWU wells.

5.2. Fault Results

We choose fault 1 as a representative fault to show the analysis steps. Fault 1 is a N-S striking fault located in the middle of the model within $y = 4,000$ m and $y = 10,000$ m (Figure 3). The fault cuts through the model in the z direction and is almost vertical. Figures 15h and 16g show the wells within a distance of 1,000 m from fault 1. There are 18 such wells, with 12 producers and 6 injectors, which started operating during the first 5,000 days of simulation. They are numbered in Figures 15h and 16g. Most of the producers started earlier while the injectors started later at approximately $t = 4,000$ day.

Given the importance of the fault pressure p_f in determining fault stability (equation (1)), we analyze the evolution of fault pressure on fault 1 across the selected time steps in Figure 14. Since there are wells on both sides of fault 1 causing pressure to change on both sides, the fault pressure within the reservoir depth interval shows a trend with time that is similar to that of the reservoir pressure in Figure 11.

Next we analyze the change in tractions on fault 1. We consider traction changes at $t = 4,500$ and 5,000 days to distinguish between production-dominated and injection-dominated effects. There are three tractions on a fault surface: lateral or along-strike shear, along-dip shear, and effective normal. The induced lateral shear on fault 1 is negligible compared to the induced dip shear and effective normal tractions. This is primarily a result of the well locations and flow rates. Reservoir contraction- or expansion-induced lateral shear around a producer or an injector cancel out when the effects are superposed over multiple wells distributed relatively uniformly in the fault blocks, which is the situation in FWU. In contrast, the dip shear and normal tractions induced by net production or injection from all the wells concentrated within a relatively thin

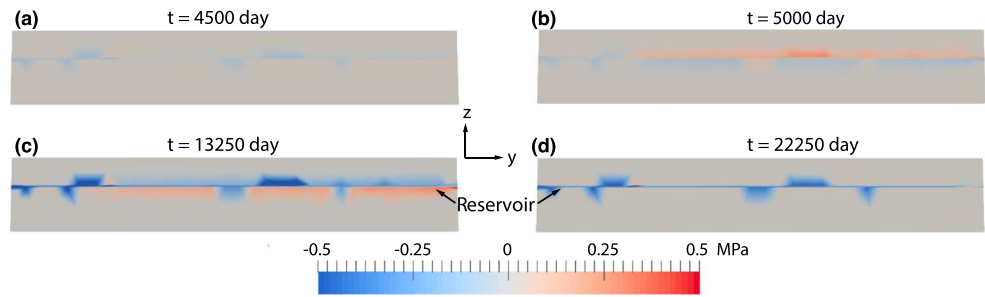


Figure 17. Changes in the Coulomb failure stress (megapascal) on fault 1 at the four selected time steps: a, b, c, and d. Red color or positive values indicate induced destabilization. Blue color or negative values indicate induced stabilization.

reservoir interval are not negligible. For example, inside the reservoir, production will induce compression near the producer and extension away from the producer (Segall & Fitzgerald, 1998). Therefore, production leads to positive (tensile) normal traction changes inside the reservoir and negative (compressive) normal traction changes in the overburden and basement (Figure 15a). Along the dip direction, production will induce downdip shear in overburden and updip shear in the basement (Figure 15b). The induced traction directions are opposite in case of injection as shown in Figure 16.

We calculate the change in ΔCFF on the faults. Positive or negative ΔCFF implies a decrease or an increase in the fault stability, respectively. The results for fault 1 are shown in Figure 17. Let's consider the reservoir domain. At the end of primary depletion of FWU, at $t = 4,500$ day, production-induced contraction causes a tensile change in the total normal traction ($\Delta\sigma_n > 0$) and an increase in the shear traction magnitude ($\Delta|\tau| > 0$) immediately adjacent to the reservoir. The fault pressure decreases inside the reservoir as shown in Figure 14. Since the magnitude of the pressure change is larger than that of the total traction change, the effective normal traction decreases. Also, the effective normal traction changes are larger than the shear traction changes given the fault dip angle. Therefore, ΔCFF is negative (stabilizing) at $t = 4,500$ day. At

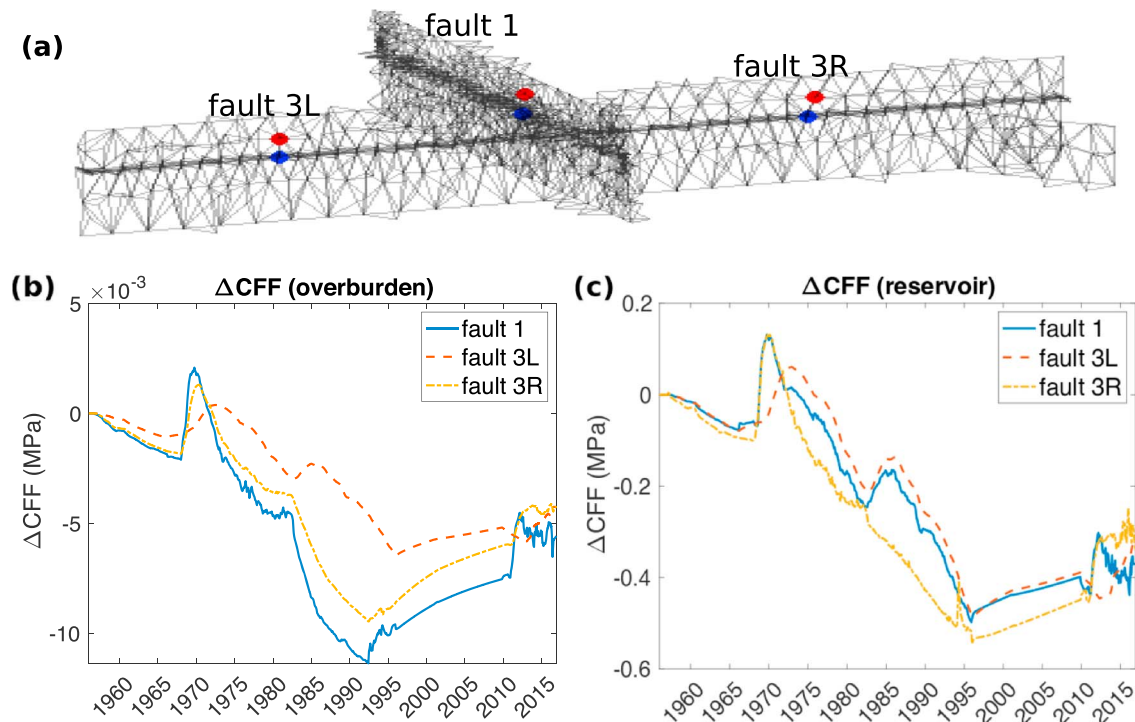


Figure 18. Evolution of ΔCFF on selected points within the overburden (b) and reservoir (c) intervals on faults 1, 3L, and 3R. Panel (a) shows the locations of the points in the reservoir interval (blue dots) and the overburden interval (red dots).

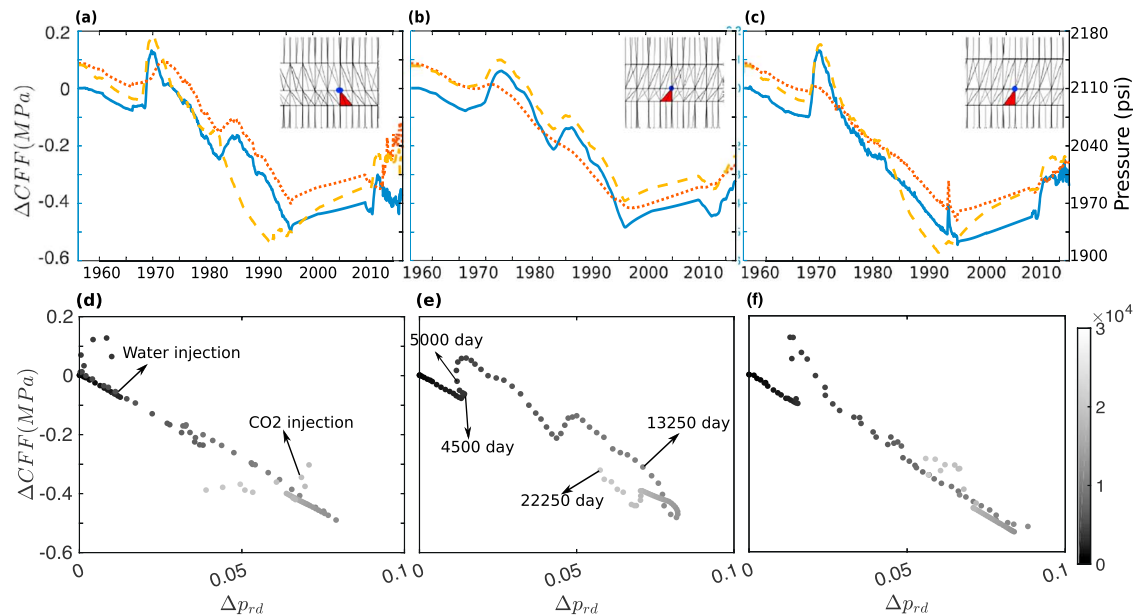


Figure 19. Comparison of ΔCFF (solid) and reservoir pressure (dotted and dashed) evolutions on (a) fault 1, (b) fault 3L, and (c) fault 3R at points within the reservoir interval. The two pressure curves are from two elements connected to the blue dot (inset) on the two sides of the fault. ΔCFF follows the trend of the larger pressure because p_f is defined from the larger of the two pressures. Plots (d), (e), and (f) show the characteristic ΔCFF versus Δp_{rd} behavior for faults 1, 3L, and 3R, respectively. Time evolution is shown through the color of the dots. The color legend on the right shows that the time evolves from $t = 0$ (black) to $t = 22,250$ day (gray). Start of water injection and CO_2 injection are marked in (d).

$t = 5,000$ day, when injection dominates, the fault pressure increases and overcomes the decrease in the total normal traction due to injection-induced expansion. Therefore, the effective normal traction increases and ΔCFF is positive (destabilizing) at $t = 5,000$ day. As production continues and the fault pressure further decreases, results similar to $t = 4,500$ day can be observed at $t = 13,250$ day. For $t > 13,250$ day, because of water and CO_2 injection, the fault pressure starts to increase but remains less than its initial value ($\Delta p_f < 0$). Therefore, an increase in ΔCFF can be observed, although it remains negative.

To understand the difference in evolution of mechanical stability within the reservoir and the overburden, we plot ΔCFF at selected points on the faults in the reservoir and the overburden interval (Figure 18). As expected, the variations are larger within the reservoir interval with a range of -0.4 to 0.1 MPa. The ΔCFF range in the overburden is much smaller: -0.017 to 0.0025 MPa. Positive (destabilizing) changes in the Coulomb stress occurs around year 1970 after water injection begins. Then it decreases and becomes negative due to production and pressure depletion. From year 1980 to 1985, the cumulative injection volume is higher than the cumulative production volume. Thus, the second peak of ΔCFF appears around year 1985 (Figure 18c). During 1995–2010, field development slowed down causing a decrease in the field production and a buildup in the field pressure and ΔCFF . Around year 2010, CO_2 injection began and ΔCFF increases accordingly. However, it remains negative.

To explain the evolution of ΔCFF and how it relates to pressure evolution, we plot ΔCFF and the element pressure together in Figures 19a to 19c for the points in the reservoir interval. For the selected point shown in the inset figure, we choose two elements in the reservoir interval from the two sides of the fault, that is, from the hanging wall and footwall blocks of the fault. Pressures from the two elements are plotted along with ΔCFF at the selected point. ΔCFF shows a general trend similar to that of the two pressures, which is expected because well operations are driving the changes in mechanical stability of the faults. However, there are two nontrivial observations. First, ΔCFF is not following either of the two pressures for the entire duration. Instead, it follows the larger of the two pressures because that defines the fault pressure p_f . The fault block with the larger pressure switches between hanging wall and footwall blocks as time evolves due to the variation in well operation with time. Second observation is that during 2011–2016 ΔCFF on fault 1 decreases while the two pressures are increasing or staying constant. In other words, ΔCFF does not seem to follow the larger pressure during this period, which corresponds to the period of CO_2 injection

and tertiary recovery in FWU. The reason is that the change in shear traction dominates ΔCFF during this period. Injection in the top reservoir layer applies downdip shear on points along the boundary between the top and bottom reservoir layers. Figure S6 confirms that $\Delta\tau_{\text{dip}}$ on the selected point decreases significantly, that is, becomes downdip, during this period, which causes ΔCFF to decrease.

Since we are interested in extracting characteristic behaviors of fault destabilization induced by well operations, we plot ΔCFF as a function of the “driving force,” that is, the reservoir pressure drop. Let $\Delta p_{rd} = |1 - (p_{\text{res}}/p_{\text{res},0})|$ be the magnitude of dimensionless change in reservoir pressure due to production or injection. Depending on the model discretization size and interwell spacing, this could be defined by averaging the pressure change over multiple grid elements in the reservoir. We plot ΔCFF versus Δp_{rd} for the three faults in Figures 19d to 19f. The characteristic trend is a straight line with a negative slope. The deviations from this trend correspond to the start of water and CO_2 injection (Figure 19d) and major changes in well operations around the fault (Figure 19e). During production-dominated period, Δp_{rd} increases, and ΔCFF decreases. Hence, points evolving downward along the trend line suggest stabilization on this plot. During injection, the reservoir pressure increases such that the pressure drop compared to the initial pressure, Δp_{rd} , decreases. ΔCFF may increase or decrease depending on the relative magnitudes of fault tractions and pressure (equation (1)). Points evolving upward along the trend line, that is, increasing ΔCFF , suggests destabilization. However, injection does not always translate into destabilization as shown by the post- CO_2 -injection gray dots evolving horizontally towards left in Figure 19d, which suggests an approximately constant ΔCFF and neutral stability during injection. A similar analysis for faults 3L and 3R shows that injection is increasing the risk of induced destabilization on these two faults. Moreover, the destabilization features on the two faults are different (gray dots jump down for fault 3L and up for fault 3R) due to different locations of the two faults with respect to the wells (refer to Figures 12c and 12d).

6. Discussion and Conclusion

We presented results from a coupled flow-geomechanical simulation study of CO_2 storage and EOR in the FWU oil field of Texas. We demonstrated a novel workflow to incorporate complex geological structure, petrophysical heterogeneity, and multiwell schedule of a real oil field producing under different recovery mechanisms—primary depletion, waterflooding, and CO_2 flooding—into a rigorous multiphase flow-geomechanics simulation framework. We applied the framework to the FWU data set to predict the geomechanical effects of fluid transport and storage on faults. The main highlights are as follows:

1. Our workflow (Figures 5 through 9) demonstrates how to use existing uncoupled models to initialize and distribute properties and wells in a coupled model. This is important because many oil fields have uncoupled, flow-only simulation models that are calibrated continually with significant effort because of their role in reporting hydrocarbon reserves and finding new drilling locations in the oil field. Finding an efficient workflow to convert them into coupled models can accelerate the adoption of the coupled modeling technology.
2. Our workflow shows how to identify and characterize geomechanical signatures of flow compartmentalization and bypassed oil due to faults, well configurations, and well rate variations. The simulated horizontal and vertical displacement fields (e.g., Figure 13) can be used to determine whether the reservoir regions, left unswept during CO_2 or waterflooding, can or cannot be detected with the aid of surface deformation data, for example, InSAR and GPS.
3. We demonstrate that we can maintain an approximately constant ΔCFF (Figure 19d) on critically oriented faults and thereby control their induced seismicity risks, by carefully managing the wells.

We tested the mesh sensitivity of the conclusions by comparing the above results with those from the refined mesh mentioned above and described in the supporting information. We observe that the refined mesh provides a higher resolution than the coarse mesh. However, the coarse mesh captures the spatial and temporal trends of pressure, displacement, and fault stresses as well as the refined mesh. This provides confidence in the conclusions of this study.

References

- Aagaard, B. T., Knepley, M. G., & Williams, C. A. (2013). A domain decomposition approach to implementing fault slip in finite-element models of quasi-static and dynamic crustal deformation. *Journal of Geophysical Research: Solid Earth*, *118*, 3059–3079. <https://doi.org/10.1002/jgrb.50217>

Acknowledgments

The support of the United States Department of Energy, National Energy Technology Laboratory through NETL-Penn State University Coalition for Fossil Energy Research (UCFER, contract DE-FE0026825) is gratefully acknowledged. Data are provided in the text and available for download from National Geoscience Data Centre (NGDC) at <http://www.bgs.ac.uk/services/ngdc/>.

- Albano, M., Barba, S., Tarabusi, G., Saroli, M., & Stramondo, S. (2017). Discriminating between natural and anthropogenic earthquakes: Insights from the Emilia Romagna (Italy) 2012 seismic sequence. *SCI. REP-UK*.
- Ampomah, W., Balch, R., Cather, M., Rose-Coss, D., Dai, Z., Heath, J., et al. (2016). Evaluation of CO₂ storage mechanisms in CO₂ enhanced oil recovery sites: Application to Morrow Sandstone Reservoir. *Energy & Fuels*, *30*, 8545–8555.
- Ampomah, W., Balch, R. S., Cather, M., Rose-Coss, D., & Gragg, E. (2017). Numerical simulation of CO₂-EOR and storage potential in the Morrow Formation, Ochiltree County, Texas. In *SPE Oklahoma City Oil and Gas Symposium*, Oklahoma City, Oklahoma.
- Ampomah, W., Balch, R. S., Cather, M., Will, R., Gunda, D., Dai, Z., & Soltanian, M. R. (2017). Optimum design of CO₂ storage and oil recovery under geological uncertainty. *Applied Energy*, *195*, 80–92.
- Ampomah, W., Balch, R. S., Ross-Coss, D., Hutton, A., Cather, M., & Will, R. A. (2016). An integrated approach for characterizing a sandstone reservoir in the Anadarko Basin. In *Offshore Technology Conference*.
- Aziz, K., & Settari, A. (1979). *Petroleum reservoir simulation*. London: Elsevier.
- Balch, R. S., McPherson, B., & Grigg, R. (2017). Overview of a large scale carbon capture, utilization, and storage demonstration project in an active oil field in Texas, USA. *Energy Procedia*, *114*, 5874–5887.
- Bissell, R. C., Vasco, D. W., Atbi, M., Hamdani, M., Okwelegbe, M., & Goldwater, M. H. (2011). A full field simulation of the in Salah gas production and CO₂ storage project using a coupled geo-mechanical and thermal fluid flow simulator. *Energy Procedia*, *4*, 3290–3297.
- Castelletto, N., Teatini, P., Gambolati, G., Bossie-Codreanu, D., Vinc  , O., Daniel, J. M., et al. (2013). Multiphysics modeling of CO₂ sequestration in a faulted saline formation in Italy. *Advances in Water Resources*, *62*, 570–587.
- Castelletto, N., White, J. A., & Tchelepi, H. A. (2015). Accuracy and convergence properties of the fixed-stress iterative solution of two-way coupled poromechanics. *International Journal for Numerical and Analytical Methods in Geomechanics*, *39*, 1593–1618.
- Castineira, D., Jha, B., & Juanes, R. (2015). Uncertainty quantification and inverse modeling of fault poromechanics and induced seismicity: Application to a synthetic carbon capture and storage (CCS) problem. 50th US Rock Mechanics/Geomechanics Symposium, Am. Rock Mech. Assoc.
- Chiaromonte, L., Zoback, M. D., Friedmann, J., & Stamp, V. (2008). Seal integrity and feasibility of CO₂ sequestration in the Teapot Dome EOR pilot: geomechanical site characterization. *Environmental Geology*, *54*(8), 1667–1675.
- Coussy, O. (2004). *Poromechanics*. Chichester, England: John Wiley and Sons.
- El-kaseeh, G., Will, R., Balch, R., & Grigg, R. (2017). Multi-scale seismic measurements for CO₂ monitoring in an EOR/CCUS project. *Energy Procedia*, *114*, 3656–3670.
- Evans, J. L. (1979). Major structural and stratigraphic features of the Anadarko basin. In N. J. Hyne (Ed.), *Pennsylvanian sandstones of the mid-continent* (pp. 97–113). Oklahoma: Tulsa Geological Society Special Publication.
- Evans, K. F., Zappone, A., Kraft, T., Deichmann, N., & Moia, F. (2012). A survey of the induced seismic responses to fluid injection in geothermal and CO₂ reservoirs in Europe. *Geothermics*, *41*, 30–54.
- Fan, Z., Eichhubl, P., & Gale, J. F. W. (2016). Geomechanical analysis of fluid injection and seismic fault slip for the Mw4.8 Timpson, Texas, earthquake sequence. *Journal of Geophysical Research: Solid Earth*, *121*, 2798–2812. <https://doi.org/10.1002/2016JB012821>
- Franklin, O. M. (2009). Onshore geologic storage of CO₂. *Science*, *325*(5948), 1656–1658.
- Garipov, T. T., Karimi-Fard, M., & Tchelepi, H. A. (2016). Discrete fracture model for coupled flow and geomechanics. *Computers & Geosciences*, *20*, 149–160.
- Hornbach, M. J., DeShon, H. R., Ellsworth, W. L., Stump, B. W., Hayward, C., Frohlich, C., et al. (2015). Causal factors for seismicity near Azle, Texas. *Nature Communications*, *6*, 6728.
- Hutton, A. (2015). Geophysical modeling and structural interpretation of a 3d reflection seismic survey in Farnsworth Unit, TX (M.S. Thesis), Department of Geophysics.
- Jagalur-Mohan, J., Jha, B., Wang, Z., Juanes, R., & Marzouk, Y. (2018). Inferring fault frictional and reservoir hydraulic properties from injection-induced seismicity. *Geophysical Research Letters*, *45*, 1313–1320. <https://doi.org/10.1002/2017GL075925>
- Jha, B., Bottazzi, F., Wojcik, R., Coccia, M., Bechor, N., Mclaughlin, D., et al. (2015). Reservoir characterization in an underground gas storage field using joint inversion of flow and geodetic data. *International Journal for Numerical and Analytical Methods in Geomechanics*, *39*, 1619–1638.
- Jha, B., & Juanes, R. (2014). Coupled multiphase flow and poromechanics: A computational model of pore pressure effects on fault slip and earthquake triggering. *Water Resources Research*, *50*, 3776–3808. <https://doi.org/10.1002/2013WR015175>
- Juanes, R., Jha, B., Hager, B. H., Shaw, J. H., Plesch, A., Astiz, L., et al. (2016). Were the May 2012 Emilia-Romagna earthquakes induced? A coupled flow-geomechanics modeling assessment. *Geophysical Research Letters*, *43*, 6891–6897. <https://doi.org/10.1002/2016GL069284>
- Kim, J., Tchelepi, H. A., & Juanes, R. (2011). Stability, accuracy and efficiency of sequential methods for coupled flow and geomechanics. *Society of Petroleum Engineers Journal*, *16*(2), 249–262.
- Lackner, K. S. (2003). A guide to CO₂ sequestration. *Science*, *300*(5626), 1677–1678.
- Lake, L. W., Johns, R., Rossen, B., & Pope, G. (2015). *Fundamentals of enhanced oil recovery*. Texas: Society of Petroleum Engineers.
- Lei, X., Huang, D., Su, J., Jiang, G., Wang, X., Wang, H., et al. (2013). Fault reactivation and earthquakes with magnitudes of up to Mw4.7 induced by shale-gas hydraulic fracturing in Sichuan Basin, China. *Nature Scientific Reports*, *7*, 7971.
- Lie, K.-A. (2016). An introduction to reservoir simulation using MATLAB: User guide for the Matlab Reservoir Simulation Toolbox (MRST). SINTEF ICT.
- Mainguy, M., & Longuemare, P. (2002). Coupling fluid flow and rock mechanics: Formulations of the partial coupling between reservoir and geomechanical simulators. *Oil & Gas Science and Technology*, *57*(4), 355–367.
- Minkoff, S. E., Stone, C. M., Bryant, S., Peszynska, M., & Wheeler, M. F. (2003). Coupled fluid flow and geomechanical deformation modeling. *Journal of Petroleum Science and Engineering*, *38*(1), 37–56.
- Olden, P., Pickup, G., Jin, M., Mackay, E., Hamilton, S., Somerville, J., & Todd, A. (2012). Use of rock mechanics laboratory data in geomechanical modeling to increase confidence in CO₂ geological storage. *International Journal of Greenhouse Gas Control*, *11*, 304–315.
- Panda, D., Kundu, B., Gahalaut, V. K., Burgmann, R., Jha, B., Asaithambi, R., et al. (2018). Seasonal modulation of deep slow-slip and earthquakes on the main Himalayan thrust. *Nature Communications*, *9*, 4140.
- Preisig, M., & Pr  vost, J. H. (2011). Coupled multi-phase thermo-poromechanical effects. case study: CO₂ injection at in Salah, Algeria. *International Journal of Greenhouse Gas Control*, *5*(4), 1055–1064.
- Reasenber, P. A., & Simpson, R. W. (1992). Response of regional seismicity to the static stress change produced by the Loma Prieta earthquake. *Science*, *255*, 1687–1690.
- Rutqvist, J., Birkholzer, J., Cappa, F., & Tsang, C.-F. (2007). Estimating maximum sustainable injection pressure during geological sequestration of CO₂ using coupled fluid flow and geomechanical fault-slip analysis. *Energy Conversion and Management*, *48*(6), 1798–1807.

- Rutqvist, J., Birkholzer, J. T., & Tsang, C.-F. (2008). Coupled reservoir-geomechanical analysis of the potential for tensile and shear failure associated with CO₂ injection in multilayered reservoir-caprock systems. *International Journal of Rock Mechanics*, *45*(2), 132–143.
- Schlumberger (2017). Eclipse 100 reference manual 2017.1 Houston.
- Segall, P. (1989). Earthquakes triggered by fluid extraction. *Geology*, *17*(10), 942.
- Segall, P., & Fitzgerald, S. D. (1998). A note on induced stress changes in hydrocarbon and geothermal reservoirs. *Tectonophysics*, *289*(1), 117–128.
- Segall, P., & Lu, S. (2015). Injection-induced seismicity: Poroelastic and earthquake nucleation effects. *Journal of Geophysical Research: Solid Earth*, *120*, 5082–5103. <https://doi.org/10.1002/2015JB012060>
- SpaceClaim, A. (2018). De-featuring model for CAE. Retrieved 2018-04-30, from www.spaceclaim.com/en/Solutions/ModelingForCAE/defeaturing_CAE.aspx
- Streit, J. E., & Hillis, R. R. (2004). Estimating fault stability and sustainable fluid pressures for underground storage of CO₂ in porous rock. *Energy*, *29*(9), 1445–1456.
- Szulczewski, M. L., MacMinn, C. W., Herzog, H. J., & Juanes, R. (2012). Lifetime of carbon capture and storage as a climate-change mitigation technology. *Proceedings of the National Academy of Sciences of the United States of America*, *109*(14), 5185–5189.
- Teatini, P., Castelletto, N., & Gambolati, G. (2014). 3D geomechanical modeling for CO₂ geological storage in faulted formations. A case study in an offshore northern Adriatic reservoir, Italy. *International Journal of Greenhouse Gas Control*, *22*, 63–76.
- Trelis (2017). User documentation 16.1. CSimSoft.
- Verdon, J. P., Kendall, J.-M., White, D. J., & Angus, D. A. (2011). Linking microseismic event observations with geomechanical models to minimise the risks of storing CO₂ in geological formations. *Earth and Planetary Science Letters*, *305*(1), 143–152.
- Vidal-Gilbert, S., Nauroy, J.-F., & Brosse, E. (2009). 3D geomechanical modelling for CO₂ geologic storage in the Dogger carbonates of the Paris Basin. *International Journal of Greenhouse Gas Control*, *3*(3), 288–299.
- Vidal-Gilbert, S., Tenthorey, E., Dewhurst, D., Ennis-King, J., Ruth, P. V., & Hillis, R. (2010). Geomechanical analysis of the Naylor Field, Otway Basin, Australia: Implications for CO₂ injection and storage. *International Journal of Greenhouse Gas Control*, *4*(5), 827–839.
- White, M. D., Esser, R. P., McPherson, B. P., Balch, R. S., Liu, N., Rose, P. E., et al. (2017). Interpretation of tracer experiments on inverted five-spot well-patterns within the western half of the Farnsworth Unit Oil Field. *Energy Procedia*, *114*, 7070–7095.
- Won, C. K., & Paul, S. (2016). Seismicity on basement faults induced by simultaneous fluid injection-extraction. *Pure and Applied Geophysics*, *173*(8), 2621–2636.
- Won-Young, K. (2013). Induced seismicity associated with fluid injection into a deep well in Youngstown, Ohio. *Journal of Geophysical Research: Solid Earth*, *118*, 3506–3518. <https://doi.org/10.1002/jgrb.50247>
- Yang, Z., & Juanes, R. (2018). Two sides of a fault: Grain-scale analysis of pore pressure control on fault slip. *Physical Review E*, *97*, 022906.
- Yerkes, R. F., & Castle, R. O. (1976). Seismicity and faulting attributable to fluid extraction. *Engineering Geology*, *10*(2), 151–167.